Resolvent analysis of co-existing periodic-flow solutions around a NACA0012 airfoil

O. Marquet[1], J.S. Leontini [2], J. Zhao[3] and M.C. Thompson[3]

[1] ONERA/DAAA, Paris Saclay University, 92190 Meudon, France

[2] Swinburne University of Technology, Hawthorn, Victoria, 3122, Australia.

[3] Fluids Laboratory for Aeronautical and Industrial Research (FLAIR), Department of Mechanical and Aeropapce Engineering, Monash University, Melbourne, VIC 3800, Australia Australia

Abstract

At $Re = 5000$, both experiments and two-dimensional simulations of a NACA0012 airfoil wake show that, as the angle-of-attack is increased, there is a steep rise in lift beyond approximately 5° as vortex shedding begins to occur. Simulations show that the unsteady flow displays different frequencies in its saturated state between 7° and 8°, although periodic at higher and lower Reynolds numbers. Indeed, within this range, the lift signal shows multiple states and period-doubling, as the wake undergoes a substantial change in character from the standard von-Kármán vortex street. Direct simulations and resolvent analysis are used to investigate the transitions further, with the latter well predicting the observed wake frequencies and co-existing periodic states.

Keywords
Multiple periodic solution; Airfoil flows; Resolvent analysis;

Introduction

Some recent studies that have investigated low-Reynolds-number flows around airfoils include [1, 2, 3]. These have reported a complex series of wake modes depending on Reynolds number (Re) and angle-of-attack (α). Features of these modes include pairing of vortices in the wake, quasi-periodic modes and the transition to chaotic states via period-doubling. Those studies have mostly focused on higher α and lower Re. In this study, we focus on wake bifurcations at relatively low α at a moderate Reynolds number of $Re = 5000$, where the wake undergoes a series of transitions over a small α range. These transitions are analysed using resolvent analysis.

Experiments

The experiments were conducted in the free-surface recirculating water channel of the *Fluids Laboratory for Aeronautical and Industrial Research* (FLAIR) at Monash University. A machined aluminium NACA0012 airfoil model had a chord length of $c = 30 \pm 0.010$ mm and an immersed length of $L = 300$ mm, giving an aspect ratio of $L/c = 10$. The airfoil was attached to a micro-stepping motor, allowing the angle-of-attack to be set to within $\pm 0.2°$. The opposite free end of the foil was positioned with a clearance of ~ 1 mm above a conditioning platform to reduce end effects. The flow structure around the foil was measured using Particle Image Velocimetry (PIV). Figure 1 shows two instantaneous PIV vorticity plots of the wake as α is increased from 5° to 6°. Further details can be found in [4].

Direct numerical simulations

The incompressible flow is described through the non-dimensional velocity $\boldsymbol{u}$ and kinematic pressure p fields that sat-
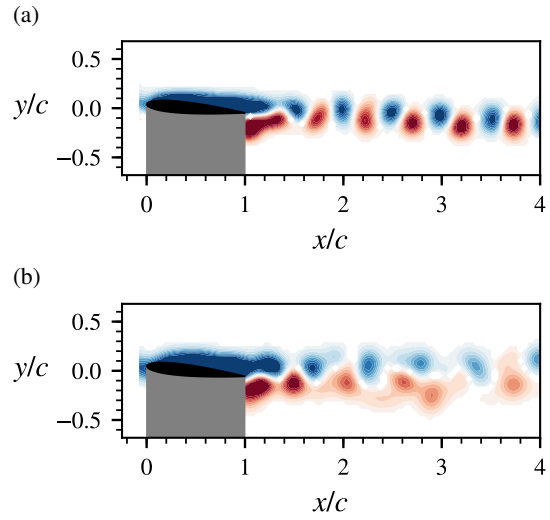

(a)

(b)

Figure 1. Experimental results at $Re = 5000$. PIV snapshots (vorticity) showing the change in the wake topology when increasing the angle-of-attack from (a) $\alpha = 5°$ to (b) $\alpha = 6°$.

isfy the Navier-Stokes equations

$$\frac{\partial \boldsymbol{u}}{\partial t} + (\boldsymbol{u} \cdot \boldsymbol{\nabla}) \boldsymbol{u} = -\boldsymbol{\nabla}p + \frac{1}{Re}\boldsymbol{\Delta u} \ , \ \boldsymbol{\nabla} \cdot \boldsymbol{u} = 0, \qquad (1)$$

where $Re = U_\infty c/\nu$ is the Reynolds number based on the chord c of a NACA0012 profile and the incoming uniform velocity U_∞. The equations are discretised in space using a finite-element method and marched in time with an implicit temporal discretisation. A second-order extrapolation of the convective velocity in the non-linear term yields a linear Oseen problem [5] that is solved here using a direct sparse LU solver. Denoting α as the angle-of-attack, the above equations are solved subject to Dirichlet boundary conditions $(u, v) = (\cos(\alpha), \sin(\alpha))$ at the inlet and lateral boundaries of the computational domain. The domain size is $10c$ in each direction. A free-stress boundary condition is imposed at the outlet. Flow solutions have been computed for the Reynolds number of $Re = 5000$. First, periodic solutions are computed for several values of the angle-of-attack in the range $5° \leq \alpha \leq 9°$ starting from a uniform velocity field as an initial condition. After identifying different branches of solutions, each branch is continued by increasing (or decreasing) the angle-of-attack, using the previously computed solution as the initial condition. The integration time is systematically adapted so as to reach the asymptotic flow state.

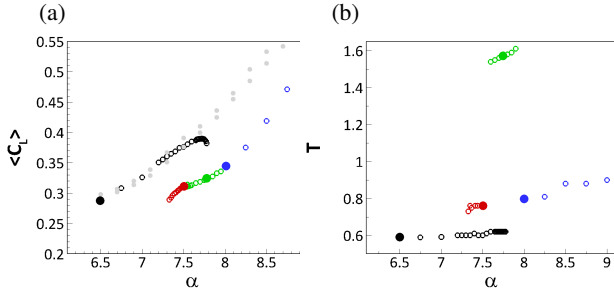The time-averaged $< C_L >$ and period T of the lift coefficient

Figure 2. (a) Time-averaged $< C_L >$ and (b) period T of the lift coefficient as a function of α. The four branches of numerical solutions are identified by black, red, green and blue open circles. The experimental results are shown with grey open circles. Filled circles identify solutions displayed in subsequent figures. Here, $Re = 5000$.

are displayed as a function of angle-of-attack in figures 2(a) and (b), respectively. Four branches of periodic solutions are identified in the range $6.5° \leq \alpha \leq 9°$. For the first branch of solutions (black circles), the mean lift coefficient increases with the angle-of-attack until $\alpha = 7.78°$ where it ceases to exist. It is in very good agreement with the time-averaged lift coefficients measured in the experiments (grey dots). A typical snapshot of the vorticity field is displayed in figure 3(a) for $\alpha = 6.5°$. A von-Kármán vortex street is observed in the wake of the foil, with clockwise (blue) and anti-clockwise (red) vortices that are periodically shed at the trailing edge. The period of this shedding is equal to $T = tU_\infty/c = 0.6$ and barely changes with α. The temporal fluctuation of the aerodynamic coefficients induced by vortex shedding is shown in figure 3(d), by displaying the instantaneous lift $C_L(t)$ as a function of the instantaneous $C_D(t)$ drag. The trajectory approximates a straight line for the angle $\alpha = 6.5°$ (black curve).

When increasing the angle-of-attack above $\alpha = 8°$, we obtain a second branch of periodic solutions shown by the blue circles in figure 2, characterised by a mean lift coefficient increasing linearly with α. The temporal evolution of the aerodynamic coefficients in figure 3(d) now resembles an ellipse and shows that the fluctuations are of larger amplitude. The period of the oscillation is also larger with $T \sim 0.8$. The vortex street displayed in figure 3(c) has deviated upwards and the distance between two vortex pairs (solid line) is larger than the distance between the two counter-rotating vortices (dashed line), unlike the situation for the classical vortex street in figure 3(a). This second periodic branch of the solution exists for large α, with the period increasing to $T = 0.9$ for $\alpha = 9°$, but it ceases to exist for angles below $\alpha = 8°$.

A third branch of periodic solution (red circles in figure 2) is obtained in the range $7.33° < \alpha \leq 7.5°$. The pattern of the vortex street (figure 3(b) has now deviated downwards. The vortex-shedding at period $T = 0.75$ is characterized by lower lift and drag coefficients, as well as fluctuations of smaller amplitude oscillation compared with the second branch (blue).

Finally, for intermediate values of angle-of-attack, $7.5° < \alpha \leq 8°$, we obtain a branch of solutions (green circles in figure 2) characterized by much larger periods in the range $1.5 \leq T \leq 1.6$. The maximal (resp. minimal) value of the period is twice the period of the blue (resp. red) branch equal to $T = 0.8$ (resp. $T = 0.75$). The instantaneous vorticity is shown in figure 3(f) and 3(g) for two instants corresponding to the two maximal values of the lift. The vortex pattern is clearly less organised than for the other branches of solution, with clockwise vortices (blue) of smaller amplitude than anti-clockwise vortices (red).
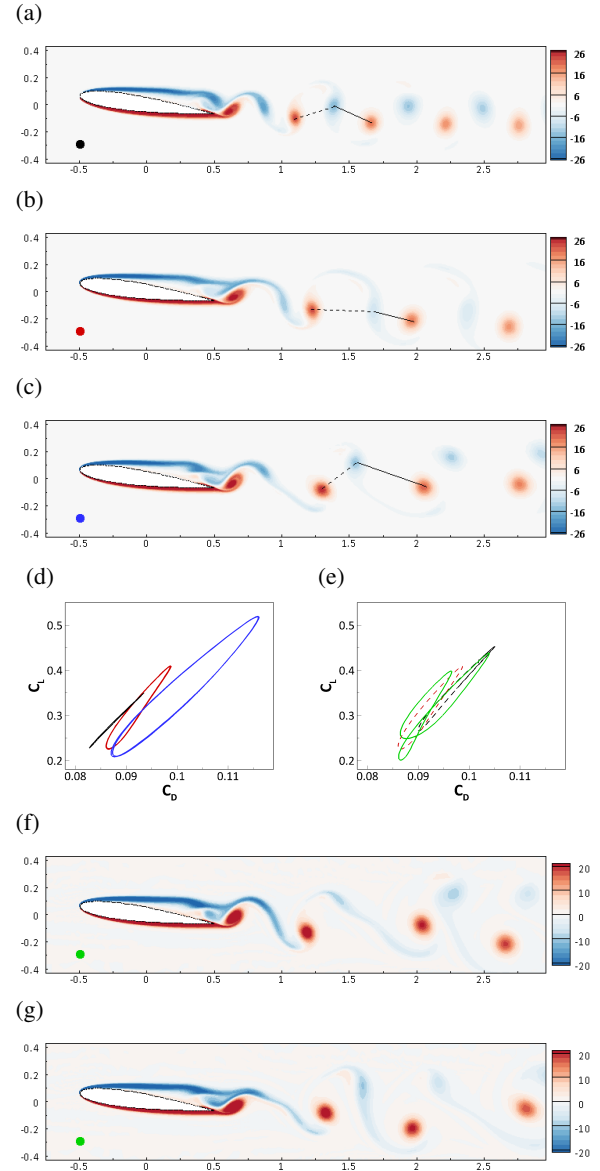

Figure 3. Isocontours of the instantaneous vorticity for the periodic solutions at (a) $\alpha = 6.5°$, (b) $\alpha = 7.5°$, (c) $\alpha = 8°$, and (f,g) $\alpha = 7.75°$ for times corresponding to the maximal lift. Their temporal evolution in instantaneous lift-versus-drag coefficients diagrams is displayed with solid curves in (d) for $\alpha = 6.5°$ (black,a), $7.5°$ (red,b) and $8°$ (blue,c), and in (e) for $\alpha = 7.75°$. In (e), the dashed curves correspond to trajectories for $\alpha = 7.5$ for the high-lift (black) and low-lift (red) solutions.

The trajectory of this solution in the lift-versus-drag diagram is now displayed in figure 3(e) with the green curve. It looks like two connected ellipses, as if the trajectories of the first (black dashed line) and second (red dashed line) branches of periodic solutions have merged, giving birth to a new periodic solution. Clearly, the existence of that low-period solution is related to the closeness of these red and black periodic solutions in phase space.

Resolvent analysis of the time-averaged flow

The resolvent analysis, introduced to capture the growth of convective instabilities developing on steady flow behaving as noise amplifiers [7], has recently received much attention for the reconstruction of fluctuations in turbulent flows [6, 8, 9, 10, 11].

Here, we analyse the time-periodic flows previously described by performing the resolvent analysis of their time-averaged (mean) flows.

Decomposing the flow velocity and pressure as the sum of the time-averaged flow fields $(\bar{\boldsymbol{u}}, \bar{p})$ and their fluctuations $(\boldsymbol{u}', p')$, and inserting this decomposition into the governing equation (1), one obtains the quasi-linear equations,

$$\frac{\partial \boldsymbol{u}'}{\partial t} + (\boldsymbol{u}' \cdot \boldsymbol{\nabla}) \bar{\boldsymbol{u}} + (\bar{\boldsymbol{u}} \cdot \boldsymbol{\nabla}) \boldsymbol{u}' + \boldsymbol{\nabla} p' - \frac{1}{Re} \boldsymbol{\Delta} \boldsymbol{u}' = \boldsymbol{f}' \ , \ \ \boldsymbol{\nabla} \cdot \boldsymbol{u}' = 0,$$
(2)

where $\boldsymbol{f}' = -\left(\boldsymbol{u}' \cdot \boldsymbol{\nabla}\right) \boldsymbol{u}' + \overline{\left(\boldsymbol{u}' \cdot \boldsymbol{\nabla}\right) \boldsymbol{u}'}$. In the resolvent analysis, this non-linear term is modelled as an external unknown forcing, yielding a linear relationship between the velocity field response and this nonlinearity [6]. The Fourier decomposition of the forcing and flow fluctuation $\boldsymbol{q}' = \left(\boldsymbol{u}', p'\right)$, defined as $\left(\boldsymbol{q}', \boldsymbol{f}'\right)(\boldsymbol{x}, t) = \left(\hat{\boldsymbol{q}}, \hat{\boldsymbol{f}}\right)(\boldsymbol{x}) \exp(i\omega t) + \text{c.c.}$, is injected into the above quasi-linear equations, yielding, after spatial discretisation, the linear input-output harmonic equation,

$$(i\omega \boldsymbol{M} - \boldsymbol{L}(\bar{\boldsymbol{u}})) \hat{\boldsymbol{q}} = \boldsymbol{M} \boldsymbol{P} \hat{\boldsymbol{f}},$$
(3)

where $\boldsymbol{L}$ denotes the discrete linearised Navier-Stokes equations, $\boldsymbol{M}$ is a mass matrix and $\boldsymbol{P}$ is a rectangular matrix introduced to prolongate the momentum forcing vector onto a vector of size $\hat{\boldsymbol{q}}$. The transpose of this matrix allows extracting the velocity vector for the flow vector, i.e. $\hat{\boldsymbol{u}} = \boldsymbol{P}^T \hat{\boldsymbol{q}}$. The resolvent operator $\boldsymbol{R}(\omega)$ is often introduced as follows,

$$\hat{\boldsymbol{u}} = \boldsymbol{P}^T \left(i\omega \boldsymbol{M} - \boldsymbol{L}(\bar{\boldsymbol{u}})\right)^{-1} \boldsymbol{M} \boldsymbol{P} \hat{\boldsymbol{f}} = \boldsymbol{R}(\omega) \hat{\boldsymbol{f}},$$
(4)

to express the linear relationship between the output harmonic velocity $\hat{\boldsymbol{u}}$ and the input harmonic forcing $\hat{\boldsymbol{f}}$. The resolvent modes are the left (response) and right (forcing) modes in a singular value decomposition of the resolvent operator. The forcing modes $\tilde{\boldsymbol{f}}_k$ may be obtained by computing the eigenmodes for the following Hermitian eigenvalue problem

$$\left(\boldsymbol{R}(\omega)^H \boldsymbol{R}(\omega)\right) \tilde{\boldsymbol{f}}_k = \lambda_k^2 \tilde{\boldsymbol{f}}_k.$$
(5)

The response modes $\tilde{\boldsymbol{u}}_k$ are then obtained as the solution of (3) with $\tilde{\boldsymbol{f}} = \tilde{\boldsymbol{f}}_k$ Assuming that the forcing modes are normalised as $\tilde{\boldsymbol{f}}_k^H \boldsymbol{M} \tilde{\boldsymbol{f}}_k = 1$, the kinetic energies of the response modes correspond to the positive eigenvalues of the above eigenvalue problem, i.e. $\lambda_k^2 = \tilde{\boldsymbol{u}}_k^H \boldsymbol{M} \tilde{\boldsymbol{u}}_k$. Ranking the eigenmodes in decreasing order of kinetic energy ($\lambda_0^2 > \lambda_1^2 > \cdots$), the leading modes (of largest energy gain) have been used to reconstruct the flow fluctuations (see for instance [8]).

The resolvent analysis is first performed for the mean-flow of the periodic solution at $\alpha = 6.5°$ displayed in figure 3(a). Figure 4(a) shows the energy gain of the leading modes as a function of the forcing period $2\pi/\omega$. A peak is clearly observed around the forcing period 0.62, close to the flow period of 0.6. The real part of the resolvent mode corresponding to that forcing period is displayed in figure 5(a) with isocontours of vorticity. The oscillating pattern in the streamwise direction is typical of vortex shedding. However, a comparison with the pattern of the fundamental harmonic of the periodic solution, shown in figure 5(b), reveals different shapes in the cross-stream direction, the latter being more spread. For that angle-of-attack, the resolvent analysis well identifies the oscillating frequency of the periodic solution, but it does not perfectly capture the spatial structure of the fundamental harmonic.

We now turn to results of the resolvent analysis performed for the angle-of-attack $\alpha = 7.5°$, for which we recall that two periodic solutions co-exist, a high-lift solution (black circles in

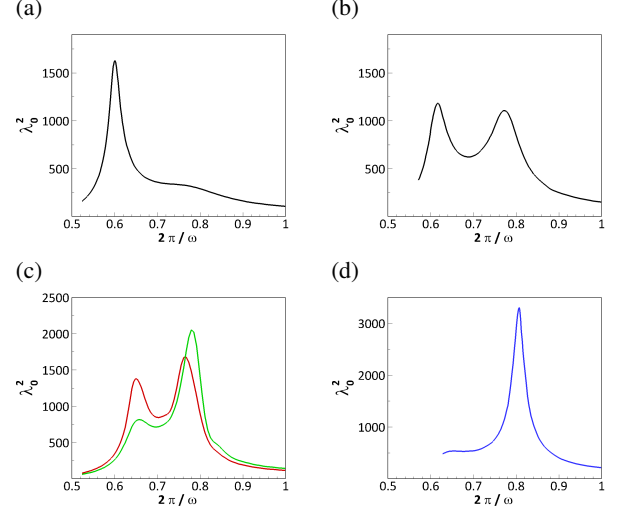Figure 4. Resolvent analysis of the time-averaged flow solutions for (a) $\alpha = 6.5°$, (b) $\alpha = 7.5°$ (high-lift branch), (c) $\alpha = 7.5°$ (low-lift branch, red) and $\alpha = 7.75°$ (low-lift branch, green), and (d) $\alpha = 8°$. The energetic gain λ_0^2 of the leading resolvent modes is displayed as a function of the forcing period $2\pi/\omega$.
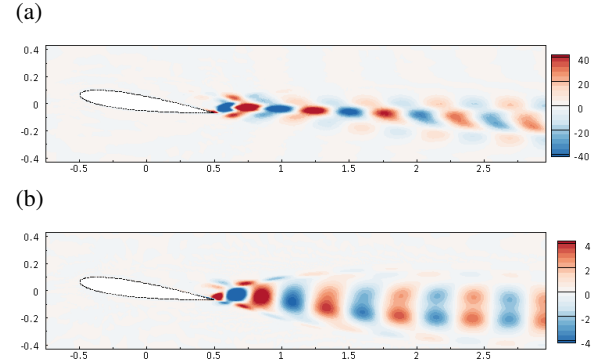
Figure 5. (a) Resolvent mode, and (b) fundamental harmonic of the periodic flow at $\alpha = 6.5°$. The resolvent mode corresponds to the energy peak in figure 4(a) for the forcing period $2\pi/\omega = 0.61$. The fundamental harmonic oscillates at period $T = 0.6$.

figure 2) and a low-lift solution (red circles). The energy gains are displayed in figure 4(b) and (c), respectively, identified by the same colors. Although both solutions are periodic (and thus characterised by one fundamental frequency), we observe two peaks in the resolvent analysis (in both cases). The first one is obtained for the forcing period $2\pi/\omega = 0.6 - 0.65$ is close to the period of the high-lift periodic solution. The second peak obtained for the forcing period $2\pi/\omega = 0.76 - 0.78$ is close to the period of the low-lift periodic solution. These two peaks are also obtained for the resolvent analysis of the doubling-period solution (green) and the sum of the forcing period is now close to the flow period $T = 1.6$. No peak of energy is obtained at this forcing period.

These two peaks clearly indicate the existence of two mechanisms of linear amplification, similarly to [10] for the flow around an airfoil at higher Reynolds number $Re = 10\,000$ and angle-of-attack $\alpha = 10.5°$. However, in the present case, the two peaks are associated with similar frequencies and related to the amplification of wake instabilities, not to Kelvin-Helmholtz instabilities in the shear layer. Clearly, when the two periodic

solutions are getting close in the phase space (see Figure 3(e)), the resolvent analysis of the mean flow reveals the existence of both linear mechanisms characterising each periodic solution. As noted for $\alpha = 6.5°$, the resolvent response shown in figure 6(a) does not perfectly compare to the fundamental harmonic shown in figure 6(b). Finally, when increasing the angle-of-
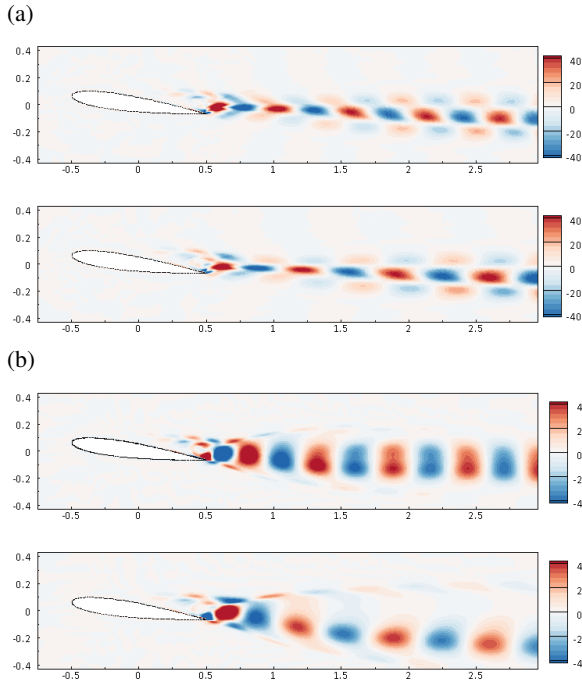
(a)

(b)

Figure 6. (a) Resolvent mode of the high-lift periodic solution, and (b) fundamental harmonics of the high-lift (top) and low-lift (bottom) periodic solutions at $\alpha = 7.5°$. The resolvent modes in (a) corresponds to the two energy peaks in figure 4(b) for the forcing period (top) $2\pi/\omega = 0.61$ and (bottom) $2\pi/\omega = 0.76$. The fundamental harmonics in (b) oscillate at the periods (top) $T = 0.61$ and (bottom) $T = 0.76$.

attack to $\alpha = 8°$, only the high-frequency peak of energy remains in figure 4(d), corresponding to the flow period. The response mode displayed in figure 7(a) does not so well approximate the fundamental harmonic shown in figure 7(b). This discrepancy is probably due to the higher-harmonics terms (somehow neglected in the resolvent analysis since embedded in the linear forcing $\boldsymbol{f'}$), that play a role in transferring the energy between different flow harmonics [12].

Acknowledgements

References

[1] Rossi, E., Colagrossi, A., Oger, G., and Le Touzé, D. (2018). Multiple bifurcations of the flow over stalled airfoils when changing the Reynolds number. *Journal of Fluid Mechanics*, 846, 356–391 (DOI:10.1017/jfm.2018.189).

[2] Kurtulus, D.F. (2016). On the wake pattern of symmetric airfoils for different incidence angles at Re=1000. *International Journal of Micro Air Vehicles*, 8(2), 109–139
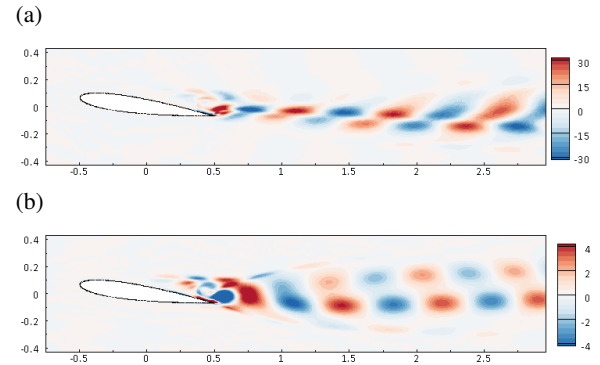
(a)

(b)

Figure 7. (a) Resolvent mode, and (b) fundamental harmonic of the periodic flow at $\alpha = 8°$. The resolvent mode corresponds to the energy peak in figure 4(d) for the forcing period $2\pi/\omega = 0.81$. The fundamental harmonic oscillates at period $T = 0.8$.

[3] Khalid, M.S.U., and Akhtar, I. (2012). Characteristics of flow past a symmetric airfoil at low Reynolds number: a nonlinear perspective. in *Proc. 2012 ASME International Mechanical Engineering Congress ad Exposition*, Houston, Texas, USA, Paper IMECE2012-87389.

[4] Zhao, J., Lo Jacono, D., Sheridan, J., Hourigan, K., & Thompson, M. C. (2018). Experimental investigation of in-line flow-induced vibration of a rotating circular cylinder. *Journal of Fluid Mechanics*, 847, 664-699.

[5] John, V. (2016). Finite element methods for incompressible flow problems. Cham: Springer International Publishing.

[6] McKeon, B. J., & Sharma, A. S. (2010). A critical-layer framework for turbulent pipe flow. Journal of Fluid Mechanics, 658, 336-382.

[7] Sipp, D., & Marquet, O. (2013). Characterization of noise amplifiers with global singular modes: the case of the leading-edge flat-plate boundary layer. *Theoretical and Computational Fluid Dynamics*, 27(5), 617-635.

[8] Beneddine, S., Yegavian, R., Sipp, D., & Leclaire, B. (2017). Unsteady flow dynamics reconstruction from mean flow and point sensors: an experimental study. *Journal of Fluid Mechanics*, 824, 174-201.

[9] Thomareis, N., & Papadakis, G. (2018). Resolvent analysis of separated and attached flows around an airfoil at transitional Reynolds number. *Physical Review Fluids*, 3(7), 073901.

[10] Symon, S., Sipp, D., & McKeon, B. J. (2019). A tale of two airfoils: resolvent-based modelling of an oscillator versus an amplifier from an experimental mean. *Journal of Fluid Mechanics*, 881, 51-83.

[11] Lesshafft, L., Semeraro, O., Jaunet, V., Cavalieri, A. V., & Jordan, P. (2019). Resolvent-based modeling of coherent wave packets in a turbulent jet. *Physical Review Fluids*, 4(6), 063901.

[12] Jin, B., Symon, S., & Illingworth, S. J. (2020). Energy transfer mechanisms and resolvent analysis in the cylinder wake. arXiv preprint arXiv:2004.14534.